

## RESEARCH PAPER

## THE MICROSTRUCTURE EVOLUTION AND HARDNESS IMPROVEMENT OF GRAY CAST IRON BY ADDITION OF FeSiMg FOLLOWED BY FLAME HARDENING PROCESS

Agung Setyo Darmawan<sup>1</sup>\*, Agus Dwi Anggono<sup>1</sup>, Agus Yulianto<sup>1</sup>, Bambang Waluyo Febriantoko<sup>1</sup>, Masyrukan<sup>1</sup>

<sup>1</sup>Department of Mechanical Engineering, Faculty of Engineering, Universitas Muhammadiyah Surakarta, Jl. A. Yani, Mendungan, Pabelan, Kartasura, Sukoharjo, Jawa Tengah 57162, Indonesia

\*Corresponding author: [Agung.Darmawan@ums.ac.id](mailto:Agung.Darmawan@ums.ac.id), tel.: +6281393886305, Faculty of Engineering / Universitas Muhammadiyah Surakarta, 57162, Surakarta, Jawa Tengah, Indonesia

Received: 21.04.2023

Accepted: 11.07.2023

## ABSTRACT

The addition of magnesium alloy elements followed by a flame-hardening process will change the phase configuration in gray cast iron. This study aims to investigate changes in microstructure and hardness due to these two processes. The addition of magnesium is conducted by adding FeSiMg as a carrier for magnesium. Metallographic examination to observe changes in microstructure was carried out using a Scanning Electron Microscope (SEM) and Energy-Dispersive X-ray Spectroscopy (EDS). The formed phase is examined by X-ray diffraction testing. The hardness test was carried out using the Vickers technique on the surface of the gray cast iron, the nodular cast iron, and the flame-hardened nodular cast iron. Whilst for flame-hardened nodular cast iron, the Vickers technique was also conducted on a cross-section. The addition of the FeSiMg compound changed flake graphite into spherical graphite with increased hardness from 130 HV to 313.22 HV. The flame-hardening process in nodular cast iron results in the formation of a martensite phase and the disappearance of graphite on the surface of the material. The hardness on the surface of the material due to the flame-hardening process increased by 82.4% compared to the substrate.

**Keywords:** Flame Hardening; Gray Cast Iron; Magnesium; Nodular Cast Iron

## INTRODUCTION

Gray cast iron (GCI) plays an important role in many technologies and industrial fields due to its high castability, excellent wear resistance and shock absorption, low cost, convenient machining characteristics, a wide range of possible mechanical properties, and other excellent qualities. However, GCI's wear performance, hardness, strength, and corrosion resistance, on the other hand, are all severely reduced under extreme service conditions [1-5].

Graphite lamellas distributed in the ferrous matrix describe the microstructure of GCI. The foundry technique can influence the nucleation and development of graphite flakes, allowing the required characteristics to be enhanced by size and type [6]. GCI has a coarser grain and a worse surface quality, which shortens its service life and limits its applicability. Because graphite behaves as a notch for stress concentration, grey cast iron with three-dimensional sharp flakes is brittle and weak in tension [7]. Aiming to overcome these weaknesses, the addition of alloying elements and heat treatment is carried out to improve performance. The elements that are often alloyed into gray cast iron to improve their properties are manganese [8], sulfur [9], niobium [10-12], copper [13], molybdenum [14], silicon [15], and chromium [16]. Improved properties are also carried out by modifying the phase through processes such as quenching-tempering [17], austempering [18], spheroidizing [19], laser surface treatment [20], and flame hardening [21].

Changing the shape of sharp flake graphite into spherical graphite will reduce the stress concentration so that the cast iron becomes stronger and harder. This can be accomplished by adding

magnesium or cerium alloying elements [22-24]. Magnesium is the most used nodular forming element, and it is usually used in alloys with other components, such as FeSiMg alloys, where the other elements act to minimize the violent reaction between magnesium and the base iron, as well as to control matrix composition and minimize the effect of damaging elements on graphite morphology. Excessive magnesium and cerium concentration can result in carbides and exploding or degenerate graphite, thus it's critical to use the right amounts of the nodularizing compounds. [25].

Nodular cast iron (NCI) has several advantages, including excellent ductility, strength, shock resistance, corrosion resistance, and wear resistance [26, 27]. Automotive (crankshaft, connecting rods, piston, etc.), wind power (hubs, machine frames, etc.), and food sectors (pans, baking plates, etc.) have all turned to NCI to meet their component requirements [28]. NCI is a cost-effective material for low to mid-range stressed components in a variety of applications due to its improved castability, machinability, and high recycling efficiency [29].

Flame-hardening is a heat treatment process used to increase the hardness of metal surfaces. Thamilarasan et al. in 2021 [30] carried out a flame-hardening process on low-carbon steel using an oxy-acetylene flame. The microhardness results were evaluated. The maximum microhardness value of 600 HV to 700 HV was obtained by manipulating the torch cap from 25 mm to 35 mm with an austenitizing temperature of 900 °C.

Hardness is an important mechanical property of engineering materials [31-34]. These mechanical properties have a direct relationship with the microstructure [35, 36]. The novelty of this research was the addition of 200 g of FeSiMg compound into 15

Kg of gray cast iron liquid, followed by flame-hardening to increase the surface hardness of metal surfaces. Therefore, the purpose of this study was to determine the effect of adding FeSiMg followed by flame hardening on the microstructure and hardness of gray cast iron. Investigations were carried out on changes in microstructure and hardness.

## MATERIAL AND METHODS

The material used in this research was gray cast iron. The gray cast iron of 15 Kg was melted with the addition of the FeSiMg compound of 200 g. This compound presents magnesium which will convert the flake graphite in gray cast iron into spherical graphite so that the gray cast iron turns into nodular cast iron. The composition test was carried out using a Brukers Q2 ION spectrometer for gray cast iron and nodular cast iron.

Metallographic testing was performed on gray cast iron and nodular cast iron using a Scanning Electron Microscope (SEM) equipped with Energy-Dispersive X-ray spectroscopy (EDS). This test was performed with SEM to observe the graphite phase and the formed matrix. The composition of the elements in the phase was also observed with EDS. The microstructure of the flame-hardened nodular cast iron was observed with an optical microscope. Further observations with this EDS were confirmed with an X-ray diffraction (XRD) tool to ascertain the type of phases formed on both cast irons.

The flame-hardening process is carried out after the addition of the FeSiMg compound. The flame-hardening process used in this research is the progressive method, where the flame is directed to the place to be heated and hardened on the entire surface. When the specimen is heated, the water nozzle is also directed parallel to the movement of the torch which is called the quenching process. The flame-hardening process is carried out by utilizing a flame from a mixture of oxy-acetylene gas, while the cooling process uses pumped water.

The progressive method is used because the construction of the tool is simpler than the spinning method and the heated surface area can be larger when compared to the spot or stationary method where heating is only at one point on the surface. In addition, the surface area of the flame-hardening process required in this study is sufficient by using the progressive flame-hardening technique. The schematic drawing of the progressive flame hardening technique can be seen in Fig. 1. The flame hardening process was carried out with an oxygen pressure of 2.5 kg/cm<sup>2</sup>, an acetylene pressure of 0.7 kg/cm<sup>2</sup>, and an austenitizing temperature of 850 °C.

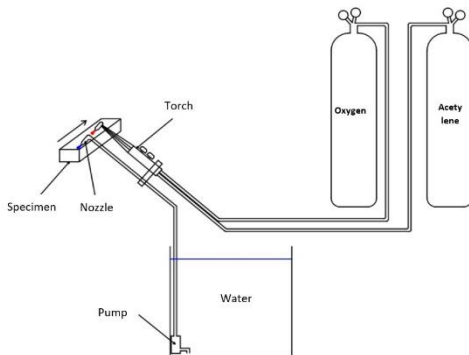


Fig. 1 Progressive flame hardening technique

Hardness testing was carried out on gray cast iron, nodular cast iron, and flame-hardened nodular cast iron. Gray cast iron and nodular cast iron hardness testing were carried out on the surface

using the macro-Vickers technique based on the ASTM E92 Standard Test Method. The flame-hardened nodular cast iron hardness test was also carried out using the micro-Vickers technique based on the ASTM E384 Standard Test Method on a cross-section from the surface to the substrate.

## RESULTS AND DISCUSSION

### Addition of FeSiMg compound

The compositions of the cast iron before (gray cast iron) and after (nodular cast iron) the addition of FeSiMg compounds are shown in Table 1. The addition of FeSiMg compounds resulted in the presence of the element magnesium. The composition of magnesium was recorded at 0.0351%. This element of magnesium changes the shape of graphite flakes to become spherical. This cast iron with spherical graphite is referred to as nodular cast iron.

Figure 2 shows metallographic and compositional test results on gray cast iron using SEM-EDS. From Fig. 2a, there were two phases in the microstructure, namely the graphite phase and the matrix phase in the form of pearlite [37-39]. The graphite phase was shown in black color, while the pearlite phase was shown in gray color. The graphite of gray cast iron in the form of flakes with both sharp ends. This graphite was evenly distributed in the pearlite matrix.

Table 1 The composition of gray cast iron and nodular cast iron

Element	Composition of gray cast iron (%)	Composition of nodular cast iron (%)
Fe	90.7948	91.9500
C	3.4255	3.4876
Si	2.4736	2.6449
S	0.0104	0.0105
P	0.0629	0.0163
Mn	0.7236	0.5748
Mg	-	0.0351
Ni	0.0521	0.0117
Cr	0.0874	0.0896
Mo	0.0100	0.0026
Cu	0.0488	1.1144
Ti	0.0211	0.0356
Sn	0.0124	0.0088
Al	0.0113	0.0130
Nb	0.0024	0.0011
V	0.0044	0.0048
Co	0.0018	0.0034
Ca	0.0222	0.0344
Zn	0.0014	0.0018

The results of the composition test with EDX/EDS on spectrum 1 are shown in Fig. 2b. Fe (ferrous) was the element with the highest composition of 92.16 wt%. Meanwhile, the other elements have the following compositions: element C (carbon) = 5.71 wt%, Si (silicon) = 1.52 wt%, Ni (nickel) = 0.46 wt%, and Ti (titanium) = 0.15 wt%. The presence of 5.71 wt% carbon indicates the presence of the Fe<sub>3</sub>C phase which mixes with ferrite to form the pearlite phase. While Fig. 2c shows the composition of test results with EDX/EDS on spectrum 2. The composition of element C in spectrum 2 reached 77.44 wt% with other elements: ferrous = 18.47 wt%, oxygen = 3.92 wt%, silicon = 0.11 wt%, and sulfur = 0.05 wt%. It shows that the phase at spectrum 2 was the graphite phase.

The graphite and pearlite phases (a mixture of ferrite and cementite) in gray cast iron were confirmed by the results of composition testing using X-Ray Diffraction as shown in Fig. 3. The presence of a graphite phase in gray cast iron was confirmed by

the appearance of a carbon element peak at an angle of 2theta of 23.38°, 44.67°, 61.98°, 76.82°, and 78.56° with intensities of 90.09 cps, 1000 cps, 34.25 cps, 35.72 cps, and 42.39 cps, respectively. The pearlite phase is confirmed by the presence of ferrite and cementite phases. The ferrite phase appears at 2theta angles of 44.67° and 64.92° with intensities of 1000 cps and 98.89 cps, respectively. The cementite phase appeared at 2theta angles of 23.38°, 44.67°, 61.98°, 64.92°, 76.82°, and 78.56° with intensities of 90.09 cps, 1000 cps, 32.45 cps, 98.89 cps, 35.72 cps, and 42.39 cps, respectively.

The gray cast iron tested consisted of two phases, namely, graphite and pearlite phases. The pearlite phase consisted of a ferrite phase and a cementite phase (Table 2). The graphite phase had a composition of 33.8 wt%, a density of 1.365 g/cm<sup>3</sup>, crystal system in the form of trigonal with cell units a = b = 2.4600 Å and c = 2.8730 Å. The ferrite phase had a composition of 39.6 wt%, a density of 7.821 g/cm<sup>3</sup>, crystal system in the form of a cubic with cell unit a = b = c = 2.8730 Å. While cementite had a composition of 26.5 wt% and a density of 7.738 g/cm<sup>3</sup>. The crystal system of cementite is orthorhombic with unit cells of a = 4.5170 Å, b = 5.0700 Å, and c = 6.7300 Å.

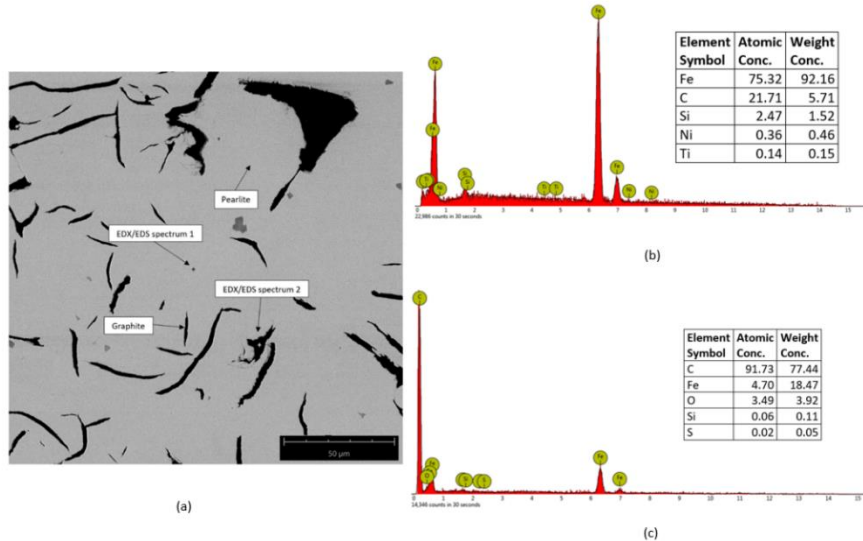


Fig. 2 Metallographic and composition test results of gray cast iron using SEM-EDS (a) Microstructure of gray cast iron, (b) Pearlite composition (c) Graphite composition

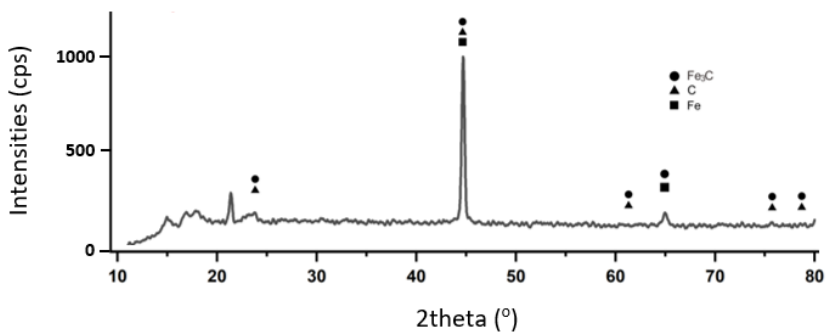
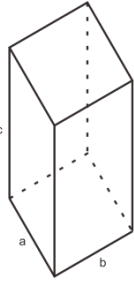
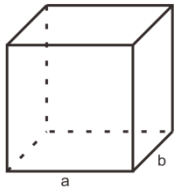
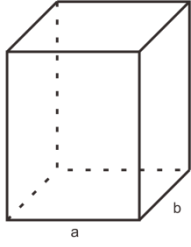


Fig. 3 Results of X-Ray Diffraction test of gray cast iron

**Table 2** Composition, density, and crystal system of gray cast iron

Phase	Composition (wt%)	Density (g/cm <sup>3</sup> )	Crystal System	Unit Cell (Å)	Crystal Structure Model
Graphite (Carbon)	33.8	1.365	Trigonal	a = b = 2.4600	
				c = 33.4500	
Ferrite (α-Ferro)	39.6	7.821	cubic	a = b = c = 2.8730	
Cementite (Fe <sub>3</sub> C)	26.5	7.738	Orthorhombic	a = 4.5170	
				b = 5.0700	
				c = 6.7300	

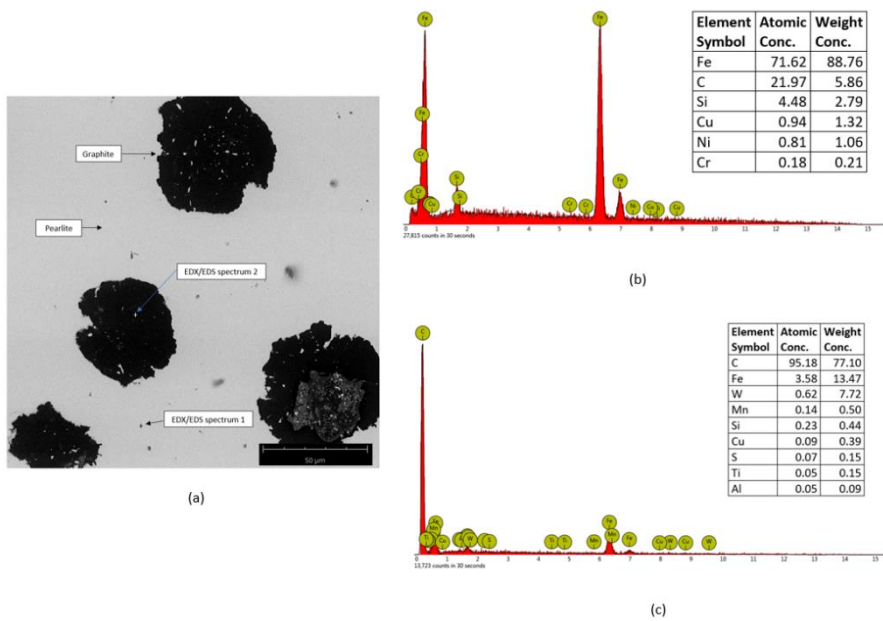
The addition of magnesium-carrying FeSiMg compounds transforms the black graphite that was originally flake-shaped into nodular-shaped (Fig. 4a). Thus, the gray cast iron also turned into nodular cast iron. The microstructure consists of spherical graphite with a pearlite matrix [40, 41].

Composition testing with EDS on graphite phase from nodular cast iron showed C = 77.10 wt%, Fe = 13.47 wt%, W = 7.72 wt%, Mn = 0.50 wt%, Si = 0.44 wt%, Cu = 0.39 wt%, S = 0.15 wt%, Ti = 0.15 wt%, and Al = 0.09 wt% (Fig. 4b). While the pearlite phase showed Fe = 88.76 wt%, C = 5.86 wt%, Si = 2.79 wt%, Cu = 1.32 wt%, Ni = 1.06 wt%, and Cr = 0.21 wt% (Fig. 4c).

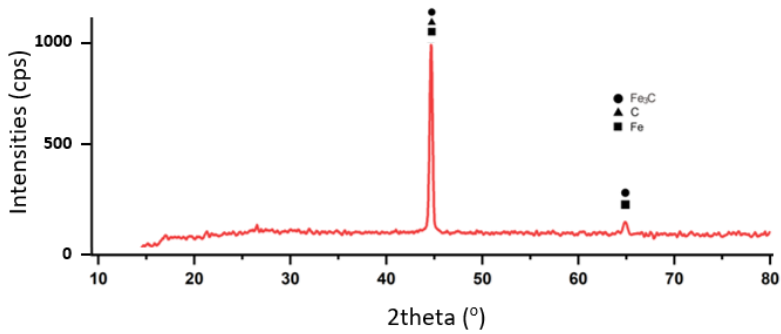
The results of composition testing using X-ray diffraction for nodular cast iron confirm that nodular cast iron (Fig. 5) also had a graphite phase surrounded by a pearlite (Ferrite + Fe<sub>3</sub>C) matrix [42]. The presence of a carbon phase was indicated by the appearance of a peak at a 2theta angle of 44.67° with an intensity of 1000 cps. The ferrite phase appeared at 2theta angles of 44.67°

and 64.92° with intensities of 1000 cps and 62.50 cps, respectively. The cementite phase appeared at 2theta angles of 44.67° and 64.92° with intensities of 1000 cps and 62.50 cps, respectively.

Table 3 shows the composition, density, and crystal system of nodular cast iron. The graphite phase had a composition of 17.8 wt%, a density of 1.365 g/cm<sup>3</sup>, crystal system in the form of trigonal with cell units a = b = 2.4600 Å and c = 33.4500 Å. The ferrite phase had a composition of 54.5 wt%, a density of 7.821 g/cm<sup>3</sup>, crystal system in the form of a cubic with cell unit a = b = c = 2.8730 Å. While cementite had a composition of 27.7 % and a density of 7.730 g/cm<sup>3</sup>. The crystal system was orthorhombic with unit cells of a = 4.5180 Å, b = 5.0690 Å, and c = 6.7360 Å. Graphite in nodular cast iron had decreased composition compared to graphite in gray cast iron. On the other hand, the pearlite composition of nodular cast iron was higher than that of gray cast iron. The crystal system of the two types of cast iron does not experience significant differences.

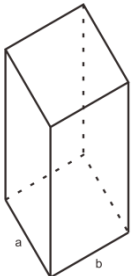
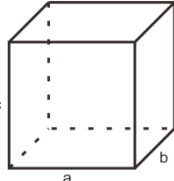
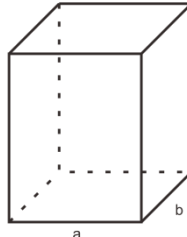


**Fig. 4** Metallographic and compositional test results of nodular cast iron using SEM-EDS (a) Microstructure of nodular cast iron, (b) Pearlite composition (c) Graphite composition



**Fig. 5** X-Ray Diffraction test results of nodular cast iron

**Table 3** Composition, density, and crystal system of nodular cast iron

Phase	Composition (wt%)	Density (g/cm <sup>3</sup> )	Crystal System	Unit Cell (Å)	Crystal Structure Model
Graphite (Carbon)	17.8	1.365	Trigonal	a = b = 2.4600	
				c = 33.4500	
Ferrite (α-Ferro)	54.5	7.821	cubic	a = b = c = 2.8730	
Cementite (Fe <sub>3</sub> C)	27.7	7.730	Orthorhombic	a = 4.5180	
				b = 5.0690	
				c = 6.7360	

#### Flame-Hardening Process of Nodular Cast Iron

The flame-hardening process is carried out after the addition of FeSiMg compounds to gray cast iron. **Figure 6** shows the changes in the microstructure from the surface to the substrate where the phase on the substrate is the same as the nodular cast iron phase before undergoing the flame-hardening process, namely in the form of pearlite and spherical graphite phases. The area affected by the flame-hardening process is divided into three zones: the martensite and retained austenite zone, the cementite and pearlite zone, and the pearlite and graphite zone.

The flame will increase the temperature to the austenitizing temperature of 850 °C where the graphite (free carbon) will diffuse into the austenite phase. Furthermore, the water spray will cool the material. This water spray causes different cooling rates on the surface of the material and the substrate. The closer to the surface, the faster the cooling rate.

In the martensite and retained austenite zones, the fast-cooling rate will result in carbon being trapped in the body center tetragonal (BCT) unit cell of ferrous to form a martensite phase [43]. Even so, not all of the austenite had the chance to transform so a retained austenite phase was formed. Retained austenite was formed due to rapid cooling of nodular cast iron that has passed

the martensite start temperature ( $M_s$ ), but has not exceeded the martensite finish temperature ( $M_f$ ). No graphite is formed in this zone.

Meanwhile, in the pearlite and cementite zones, the slower cooling rate will cause carbon to diffuse out of the austenite and combine with ferrous to form cementite. Furthermore, the austenite that is left with some carbon will form the pearlite phase. In this zone, graphite is also not formed.

The pearlite and graphite zones have the same microstructure as the raw material which does not experience flame hardening. The cooling rate in this zone is slow enough for carbon to diffuse out of the austenite. However, the presence of silicon will prevent carbon from combining with iron to form cementite so that it will become free carbon (graphite) [44].

#### Hardness Testing of gray cast iron, nodular cast iron, and flame-hardened nodular cast iron

**Figure 7** shows the results of surface hardness testing on gray cast iron, nodular cast iron, and flame-hardened nodular cast iron. The hardness value for gray cast iron was 130 HV while the hardness value for nodular cast iron was 313.22 HV. The hardness increased by 141%. The results of the hardness test on

nodular cast iron showed a higher hardness value than the hardness of gray cast iron, this was influenced by the stress that nodular cast iron can withstand became higher because the stress concentration in spherical graphite was lower than in flake graphite so that plastic deformation that can be achieved by nodular cast iron was higher [45]. Tests on the surface of flame-hardened nodular cast iron yielded a hardness value of 554.86 HV. There is an increase of 326.8% from the hardness value of gray cast iron and 77.1% from the hardness value of nodular cast iron. The increase in hardness on the surface of flame-hardened nodular cast iron is due to the formation of a hard martensite phase on the surface.

Hardness testing for flame-hardened nodular cast iron was also aimed to determine the differences in the hardness level of the material exposed to the flame-hardening process from the point closest to the torch to the substrate part of the specimen. Hard-

ness testing of the test object is carried out at 10 points. The distance of the hardness test point is starting from 0.0 mm (material's surface).

**Figure 8** shows a point at the surface having the highest hardness of 554.86 HV. The hardness decreases with increasing distance from the surface. The point at a distance of 0.5 mm from the surface has a hardness of 306.86 HV. After passing this point, the hardness did not experience a significant change. This shows that the limit of the effect of the flame-hardening process in this study is 0.5 mm from the surface. The average value of Vickers hardness on the substrate is 305.75 HV. The hardness on the surface of the material is 82.4% higher than on the substrate. The increase in hardness on the surface is caused by the formation of martensite zones and pearlite and cementite zones as shown in **Fig. 6**.

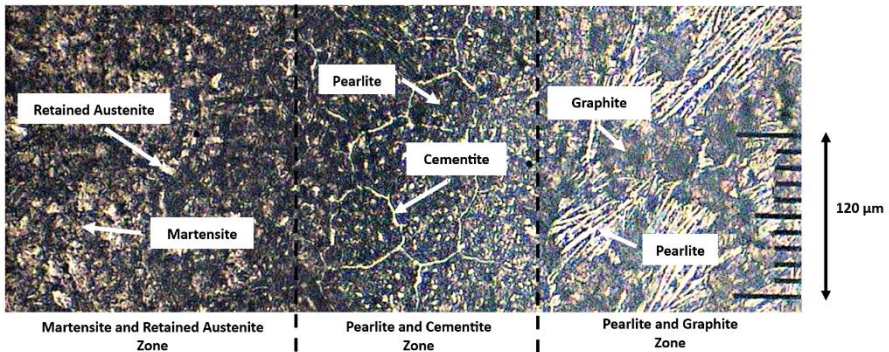


**Fig. 6** Zone of cast iron that has undergone a flame-hardening process

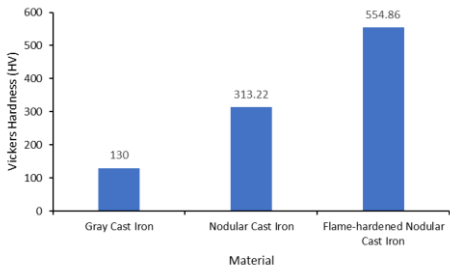


**Fig. 7** The surface hardness testing results of gray cast iron, nodular cast iron, and flame-hardened nodular cast iron

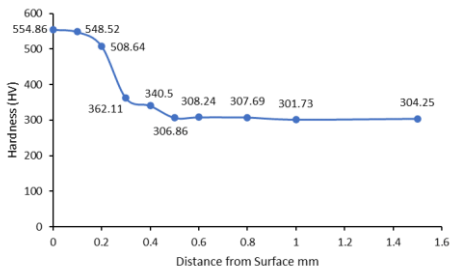


**Fig. 8** Cross-sectional hardness curve of flame-hardened nodular cast iron

## CONCLUSIONS

The addition of FeSiMg resulted in a magnesium composition of 0.0351%. The presence of this element of magnesium changes the shape of flake graphite from gray cast iron to spherical graphite so that gray cast iron turns into nodular cast iron. The hardness of cast iron is greater than that of gray cast iron. The flame-hardening process resulted in the appearance of the martensite phase and the loss of the graphite phase on the surface of nodular cast iron and increased the surface hardness of nodular cast iron by 82.4%.

**Acknowledgments:** The authors would like to acknowledge Universitas Muhammadiyah Surakarta for funding with contract number 145.3/A.3-III/LRI/VII/2022. The authors also thank the Materials Laboratory, Mechanical Engineering Department, Universitas Muhammadiyah Surakarta for facilitating mechanical and metallographic testing.

## REFERENCES

1. L. Zhu, Y. Liu, Z. Li, L. Zhou, Y. Li, A. Xiong: Optics & Laser Technology, 122, 2020, 105879. <https://doi.org/10.1016/j.optlastec.2019.105879>.
2. O. Oloyede, R. F. Cochrane, A. M. Mullis: J. Alloys Compd., 707, 2017, 347-350. <https://doi.org/10.1016/j.jallcom.2016.08.214>.
3. J. O. Olawale, J. K. Odusote, A. B. Rabi, E. O. Ochapa: J. Miner. Mater. Charact. Eng., 1(2), 2013, 44-48. <https://doi.org/10.4236/jmmce.2013.12009>.



4. S. Lee, J. H. Yu, S. H. Park, D. S. Shim, Y. S. Choi: Journal of Materials Research and Technology, 15, 2021, 189-198. <https://doi.org/10.1016/j.jmrt.2021.08.038>.
4. G. Hütter, L. Zybll, M. Kuna: Engineering Fracture Mechanics, 147, 2015, 388-397. <https://doi.org/10.1016/j.engframech.2015.06.039>.
5. L. Collini, G. Nicoletto, R. Konečná: Mater Sci Eng A, 488, 2008, 529-539. <https://doi.org/10.1016/j.msea.2007.11.070>.
7. H. Sasaki, M. Matsumoto: Materials Letters, 270, 2020, 127708. <https://doi.org/10.1016/j.matlet.2020.127708>.
8. A. Yulianto, R. Soenoko, W. Suprpto, A. Sonief: Acta Metallurgica Slovaca, 27(3), 2021, 127-132. <https://doi.org/10.36547/ams.27.3.996>.
9. R. Srivastava, B. Singh, K. K. Saxena: Materials Today: Proceedings, 26(2), 2020, 2770-2775. <https://doi.org/10.1016/j.matpr.2020.02.577>.
10. S. Weitao, W. Bin, L. Xiaoliang, W. Yuqian, Z. Jian: Tribology International, 167, 2022, 107343. <https://doi.org/10.1016/j.triboint.2021.107343>.
11. G. Beniwal, K. K. Saxena: Materials Today: Proceedings, 26(2), 2020, 2337-2343. <https://doi.org/10.1016/j.matpr.2020.02.503>.
12. H. Pourasiabi, J. D. Gates: Materials & Design, 212, 2021, 110261. <https://doi.org/10.1016/j.matdes.2021.110261>.
13. M. M. Hejazi, M. Divandari, E. Taghaddos: Materials & Design, 30(4), 2009, 1085-1092. <https://doi.org/10.1016/j.matdes.2008.06.032>.
14. S. Upadhyay, K. K. Saxena: Materials Today: Proceedings, 26(2), 2020, 2462-2470. <https://doi.org/10.1016/j.matpr.2020.02.524>.
15. K. Edalati, F. Akhlaghi, M. Nili-Ahmadabadi: Journal of Materials Processing Technology, 160, 2005, 183-187. <https://doi.org/10.1016/j.jmatprotec.2004.06.007>.
16. A. R. Zulhishamuddin, S. N. Aqida, M. M. Rashidi: Optics & Laser Technology, 104, 2018, 164-169. <https://doi.org/10.1016/j.optlastec.2018.02.027>.
17. B. Wang, Y. Pan, Y. Liu, N. Lyu, G. C. Barber, R. Wang, W. Cui, F. Qiu, M. Hu: Journal of Materials Research and Technology, 9(4), 2020, 8163-8171. <https://doi.org/10.1016/j.jmrt.2020.05.006>.
18. B. Wang, Y. Pan, Y. Liu, G. C. Barber, F. Qiu, M. Hu: Journal of Materials Research and Technology, 9(2), 2020, 2037-2043. <https://doi.org/10.1016/j.jmrt.2019.12.036>.
19. R. G. Woodward, A. Toumpis, A. Galloway: Wear, 488-489, 2022, 204155. <https://doi.org/10.1016/j.wear.2021.204155>.
20. A. Liu, B. Previtali, Physics Procedia, 5(Part A) (2010) 439-448. <https://doi.org/10.1016/j.phpro.2010.08.166>.
21. A. Yulianto, R. Soenoko, W. Suprpto, A. Sonief, A. S. Darmawan: International Journal of Emerging Trends in Engineering Research, 8(3), 2020, 617-622. <https://doi.org/10.30534/ijeter/2020/02832020>.
22. S. Banerjee, R. K. Dutta: Talanta, 27(2), 1980, 212-213. [https://doi.org/10.1016/0039-9140\(80\)80041-5](https://doi.org/10.1016/0039-9140(80)80041-5).
23. J. Lacaze, J. Sertucha, L. M. Åberg: ISIJ international, Iron & Steel Institute of Japan, 56(9), 2016, 1606-1615. <https://doi.org/10.2355/isijinternational.ISIJINT-2016-108>.
24. A. S. Darmawan, A. D. Anggono, A. Yulianto, B. W. Febriantoko, Masyrukan, A. Hamid: Key Engineering Materials, 935, 2022, 25-32. <https://doi.org/10.4028/p-2094w8>.
25. A. de Albuquerque Vicente, J. R. S. Moreno, T. F. de Abreu Santos, D. C. R. Espinosa, J. A. S. Tenório: Journal of Alloys and Compounds, 775, 2019, 1230-1234. <https://doi.org/10.1016/j.jallcom.2018.10.136>.
26. D. Kumar, M. Sauer, K. K. Ching, G. Kalss, A. C. V. D. dos Santos, G. Ramer, A. Foelske, B. Lendl, G. Liedl, A. Otto: Applied Surface Science, 559, 2021, 149897. <https://doi.org/10.1016/j.apsusc.2021.149897>.
27. A. Vaško: Materials Today: Proceedings, 32(2), 2020, 168-173. <https://doi.org/10.1016/j.matpr.2020.04.184>.
28. W. Napadtek, A. Woźniak, C. Pakowski: Tribologia, 6, 2017, 59-64. <https://doi.org/10.5604/01.3001.0010.5903>.
29. K. Hamberg, B. Johannesson, A. Robertson: Eur. Struct. Integrity Soc., 22, 1997, 37-47. [https://doi.org/10.1016/S1566-1369\(97\)80006-4](https://doi.org/10.1016/S1566-1369(97)80006-4).
30. J. Thamilarasan, N. Karunakaran, P. Nanthakumar: Materials Today: Proceedings, 46(9), 2021, 4169-4173. <https://doi.org/10.1016/j.matpr.2021.02.680>.
31. T. W. B. Riyadi: Media Mesin: Majalah Teknik Mesin, 18(1), 2017, 8-13. <https://doi.org/10.23917/mesin.v18i1.3944>.
32. N. Kholis, N. Nuryanto, A. Mustofa: Applied Research and Smart Technology, 1(2), 2020, 56-63. <https://doi.org/10.23917/arstech.v1i2.184>.
33. M. A. Hendrawan, P. I. Purboputro, A. Prima: Journal of Physics: Conference Series, 1858, 2021, 012051. <https://doi.org/10.1088/1742-6596/1858/1/012051>.
34. Wijianto, R. M. D. Ibnu, H. Adiyarini: Materials Science Forum, 961, 2019, 10-15. <https://doi.org/10.4028/www.scientific.net/MSF.961.10>.
35. A. S. Darmawan, P. I. Purboputro, B. W. Febriantoko: IOP Conf. Series: Materials Science and Engineering, 722, 2020, 012002. <https://doi.org/10.1088/1757-899X/722/1/012002>.
36. A. S. Darmawan, T. W. B. Riyadi, A. Hamid, B. W. Febriantoko, B. S. Putra: AIP Conference Proceedings, 1977, 2018, 020006. <https://doi.org/10.1063/1.5042862>.
37. P. Singhal, K. K. Saxena: Materials Today: Proceedings, 26(2), 2020, 1393-1401. <https://doi.org/10.1016/j.matpr.2020.02.281>.
38. A. Razaq, Y. Yin, J. Zhou, X. Shen, X. Ji, I. Ullah: Procedia Manufacturing, 37, 2019, 353-359. <https://doi.org/10.1016/j.promfg.2019.12.059>.
38. E. T. EL-Sawy, M. R. EL-Hebeary, I. S. E. El Mahallawi: Wear, 390-391, 2017, 113-124. <https://doi.org/10.1016/j.wear.2017.07.007>.
40. Z. Li, H. Peng, Y. Liu, X. Su, S. Kawi, J. Wang: Journal of Materials Research and Technology, 16, 2022, 1402-1412. <https://doi.org/10.1016/j.jmrt.2021.12.052>.
41. H. Wu, H. Peng, Y. Liu, H. Tu, J. Wang, X. Su: Corrosion Science, 186, 2021, 109463. <https://doi.org/10.1016/j.corsci.2021.109463>.
42. Ch. Bleicher, H. Kaufmann, T. Melz: International Journal of Fatigue, 147, 2021, 106171. <https://doi.org/10.1016/j.ijfatigue.2021.106171>.
43. R. Elliott: Cast Iron Technology, first ed., Somerset: Butterworth-Heinemann, 1988, 126-164.
44. A. C. Melado, A. S. Nishikawa, H. Goldenstein, M. A. Giles, P. A. S. Reed: International Journal of Fatigue, 104, 2017, 397-407. <https://doi.org/10.1016/j.ijfatigue.2017.07.009>.
45. J. Zou, K. Shimizu, Q. Cai: Journal of Iron and Steel Research, International, 22(11), 2015, 1049-1054. [https://doi.org/10.1016/S1006-706X\(15\)30111-4](https://doi.org/10.1016/S1006-706X(15)30111-4).
45. S. Xiang, P. Hedström, B. Zhu, J. Linder, J. Odqvist: International Journal of Fatigue, 140, 2020, 105781. <https://doi.org/10.1016/j.ijfatigue.2020.105781>.